

Contents lists available at [SciVerse ScienceDirect](http://SciVerse.Sciencedirect.com)

Planetary and Space Science

journal homepage: www.elsevier.com/locate/pss

Pit distribution in the equatorial region of Titan

Kimberly A. Adams*, Donna M. Jurdy

Department of Earth & Planetary Sciences, Northwestern University, Evanston, IL 60208-2150, USA

ARTICLE INFO

Article history:

Received 31 August 2010

Received in revised form

19 December 2011

Accepted 16 January 2012

Keywords:

Titan
Cryovolcanism
Pits
Cassini
Radar
Tectonism
Erosion
Hypsography

ABSTRACT

Cassini radar images of Titan's surface reveal numerous dark circular features in the equatorial region. These may be related to methane sublimation and have been interpreted as pits. In the T8 equatorial swath, we identify 199 individual pits and estimate their diameters. We analyze the observed spatial distribution and size to characterize these features and understand their formation. Chi-square analysis confirms a significant deviation from a random distribution and shows clustering over the entire swath. However, analysis of the densest cluster of pits, a group of 50, shows a more random distribution. Fractal analysis and comparison with a same-sized random set find only a hint of linearity. A Poisson distribution fits the observed pit-sizes, although resolution limits size determination for the smallest pits, those less than 1 km in diameter. Models for random pit generation and evolution simulate the observed Poisson distribution of pit sizes, with larger pits forming by the coalescing of smaller, overlapping ones. Pits, estimated to cover 0.5% of the equatorial T8 swath, could be an erosion mechanism that significantly contributes to the negative skew that has been observed in Titan's hypsography.

© 2012 Elsevier Ltd. All rights reserved.

1. Introduction

Titan stands out as unusual even among Saturn's diverse moons. Cassini, reaching Saturn's orbit in June of 2004, has used various instruments to penetrate Titan's thick atmosphere and image its varied surface (Elachi et al., 1991, 2004). Using Cassini's radar, and operating in synthetic aperture mode (SAR), images of Titan's surface are pieced together to give a map of radar reflectivity. Although these images have yet to cover the entire surface, they show Titan to be unique among satellites, for its varied surface features as well as its hydrocarbon chemistry and dense atmosphere, exceeding even that of Earth's.

Surprisingly Earth-like features have been revealed on Titan's surface. Lakes of methane or ethane cover the north and south pole; dried lake beds exist in the southern hemisphere (Stofan et al., 2007; Brown et al., 2008). River channels, common on the surface, may carry large amounts of liquid methane during downpours of methane rain (Tomasko et al., 2005; Perron et al., 2006; Lorenz, 2008; Lunine and Lorenz, 2009). Linear dunes are scattered over the equatorial region (Lorenz et al., 2006a,b; Radebaugh et al., 2008). Various mountain types can be seen from pole to pole (Radebaugh et al., 2007). Possible cryovolcanic features could provide methane to Titan's thick atmosphere (Lopes et al., 2007). These features, particularly the lakes and

the dense atmosphere, make Titan an exceptional satellite. All three phases of methane are stable at Titan's surface, much like the stability of water on Earth's surface. Interaction of methane cloud and liquid phases with the solid surface of Titan resembles Earth's hydrologic cycle (Atreya et al., 2006; Lorenz et al., 2003). This could account for the eerily terrestrial appearance of Titan's surface.

Titan's global topography, or hypsography, may provide clues as to the relative balance of the constructional and erosional processes acting on its surface. Indeed, Earth's characteristic bimodal hypsography was first seized upon by Alfred Wegener in 1929 to support his proposed theory of 'Continental Drift' (Wegener, 1966). Accordingly, Lorenz et al. (2011) use the limited Cassini radar topographic data to construct Titan's hypsography. They note that overall flatness characterizes Titan, and that its hypsogram is sharper than those of the terrestrial bodies. In addition, they observe that Titan's hypsography shows a distinctive skew toward lower elevations, suggestive of erosion outpacing uplift and construction through volcanism.

Pits, through their development and evolution, may represent an important – or even the dominant – erosional process on Titan. Thus we attempt to quantitatively assess the size and distribution of pits in the equatorial region. Although there are pits elsewhere on Titan, we focus on in Titan's equatorial region, between 6°–12° south and 212°–230° west, within Cassini's T8 swath where there is the largest concentration of pits. Radar dark, smooth, circular features in this area, assumed to be depressions or pits with diameters of about 1–6 km, were identified by Lopes et al. (2007).

* Corresponding author. Tel.: 1 440 552 0139.

E-mail address: ksyers@gmail.com (K.A. Adams).

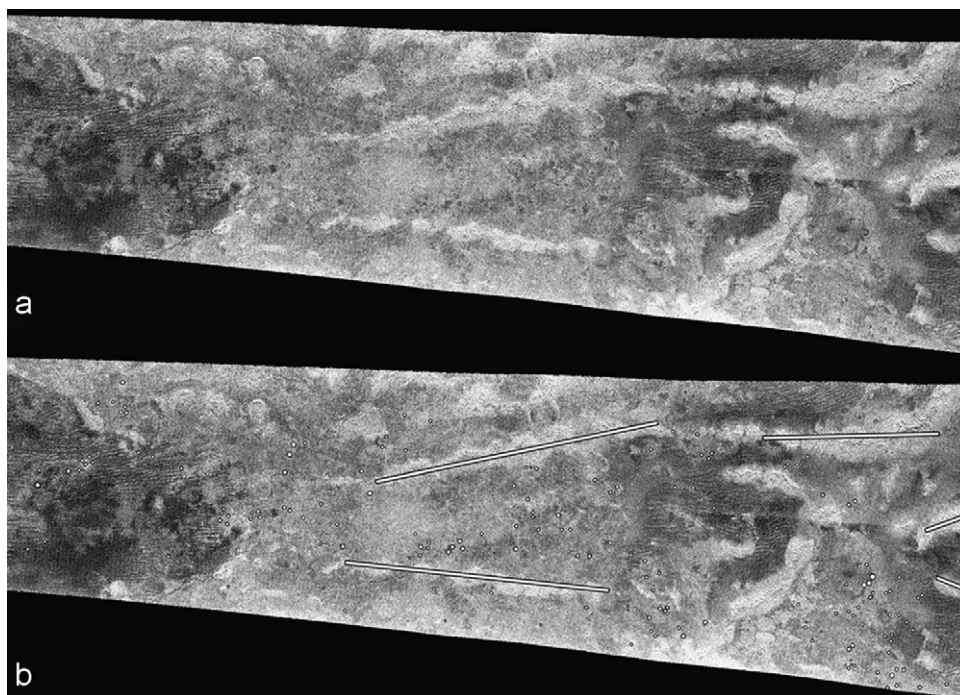


Fig. 1. Pit fields from the T8 swath that range from 1 to 6 km in diameter. These are found in the equatorial region of Titan between 6° – 12° south and 212° – 230° west. In total, 199 pits were mapped with location and diameter recorded. (a) without white circles as a reference. (b) with white circles outlined in black to highlight the pits. White lines outlined in black show linear features that continue to the east in the original T8 image.

Pits commonly occur on both icy and non-icy bodies throughout the solar system. In this paper we will consider several mechanisms for pit formation on Titan. We study the distribution and size of pits and develop quantitative models for the observations to give insight into the evolution of pits and their relationship to Titan's hypsography.

1.1. Pit formation mechanisms

Mechanisms for pit chain formation on the surface of Mars are summarized by Wyrick et al. (2004). They note the general agreement that pits form through collapse in response to a cavity beneath the surface. Methods of pit chain development include lava tubes, karst dissolution, dikes and magma chamber collapse. These mechanisms are discounted in our analysis due to the composition and state of Titan's surface. Other alternatives include extension and dilational faulting (Wyrick et al., 2004). Extension fractures can cause pit chains when collapses occur above deep fissures (Tanaka and Golombek, 1989). In this case, we would expect to find graben and other extensional features in the area. Ferrill et al. (2003) and Wyrick et al. (2004) described how dilational faulting can form pit chains similar to extensional fractures where collapses occur into voids created by such faulting.

Extension fractures seem a plausible mechanism for the development of pits on Titan due to geologic features found in the area. Radebaugh et al. (2007) have identified sub-parallel mountain ranges described as possible extension features in the region of the T8 swath that also contains the pits being studied. Fig. 1 displays these mountains (shown in Fig. 1) as radar bright, linear features, in the northern and southern part of the image. They postulate that these mountains could be formed by extensional tectonism due to their comparable width, height, and length to some mountains in the Basin and Range. Furthermore, they argue that extension commonly exists in the history of icy bodies in the solar system, and that models for Titan's outgassing

of methane produce crustal thickening and associated extension. To determine if extension is in fact the cause of pits found on Titan, we will look for linear trends.

Pits have been observed on Mars' south polar cap by the Mars Orbiter Camera on the Mars Global Surveyor (Thomas et al., 2000). Referred to as "swiss cheese" these pits have been attributed to sublimation (Thomas et al., 2000; Byrne and Ingersoll, 2003; Malin et al., 2001). Circularity of the pits are possibly due to their south polar location where a constant solar elevation causes radially symmetric ablation along the walls of depressions (MacClune et al., 2003). CO_2 ice in the south polar caps is the likely explanation for why these pits exist only in this region (MacClune et al., 2003).

Cryovolcanism was initially suggested as a method for pit development on Titan by Lopes et al. (2007). This process has been defined by Kargel (1995) as eruptions of ice-cold aqueous or non-polar molecular solutions or partly crystallized slurries that result from the partial melting of ice-bearing materials. On Titan, ice-cold refers to the surface temperature of approximately 94 K. Mitri et al. (2008) proposed cryovolcanism on Titan results from the formation of bottom crevasses in an ice-I shell floating on an ammonia-water ocean. Pockets of ammonia-water are transported to the surface through convection in the ice shell and then erupt due to re-freezing at the surface or tectonic processes (Mitri et al., 2008). Evidence of cryovolcanism can be found in Titan's atmosphere where photolysis breaks methane down to form ethane (Strobel, 1974; Yung et al., 1984). The current levels of methane in the atmosphere suggest replenishment either by large bodies of liquids on the surface or by methane out-gassing through cryovolcanism (Atreya et al., 2006; Lopes et al., 2007). With no visible cryovolcanic features in this area, such as evidence of flows or volcanic calderas, it is unlikely that this is the cause of pits in Titan's equatorial region.

Secondary craters may also cause pits on some bodies. However, no evidence of a primary crater in this area, along with Titan's thick atmosphere, make this an improbable explanation for these pits on Titan (Wood et al., 2006, 2010).

2. Mapping

Cassini radar data was utilized in our identification of pits and in their analysis. Radar swaths of Titan were obtained from the Planetary Data System operated online by NASA, with images saved as .IMG files. These are converted to .cub files using USGS ISIS program. As .cub files, images can be manipulated using various programs within ISIS or visually using the *qview* program provided by ISIS. Using *qview* the brightness and contrast can be adjusted to define features. Initially, pits were identified using a T8 image at 256 pixels per degree resolution. These pits were compared and identified using a lower resolution image at 128 pixels per degree. Pits were visually identified by looking for quasi-circular dark features that had a diameter of at least 1.05 km (three pixels in the 128 pixel/degree image). Anything smaller than three pixels was excluded due to the inability to constrain the feature's circularity. Almost certainly even smaller pits litter Titan's surface, but these cannot be identified with the current resolution. After several separate visual examinations of the T8 image we located 199 pits (Fig. 1) and determined their diameters (Table 1). Both an *a*-diameter (longest diameter) and *c*-diameter (short diameter) were found to determine the degree of circularity, or "flatness" $[(a-c)/a]$ of the pits (Table 1). Fig. 2 shows that over 90% of the pits are circular, while the remaining are nearly circular.

Table 1

Location of all pits identified in the equatorial region of Titan, latitude and longitude are given. *a*-diameters are measures of the longest diameter of the pit, while *c*-diameters measure the shortest diameter. For consistency the *a*-diameter is used for analysis. Flatness, $(a-c)/a$, is calculated for each pit to determine circularity.

Latitude	Longitude	<i>a</i> -diameter (km)	<i>c</i> -diameter (km)	Flatness (km)
-9.41	212.86	2.80	2.45	0.13
-9.56	213.10	2.80	2.80	0.00
-11.77	213.20	3.15	2.80	0.11
-10.14	213.61	3.15	2.80	0.11
-11.81	213.68	2.45	2.10	0.14
-10.20	213.69	2.10	1.40	0.33
-10.77	213.78	1.75	1.75	0.00
-10.69	213.84	2.10	2.10	0.00
-9.82	213.84	2.10	1.75	0.17
-10.64	213.90	3.50	2.80	0.20
-9.83	213.94	1.75	1.40	0.20
-11.49	213.98	3.15	2.80	0.11
-9.81	214.01	1.75	1.40	0.20
-10.49	214.04	2.45	2.10	0.14
-11.47	214.09	3.85	3.15	0.18
-11.77	214.10	3.15	3.15	0.00
-10.85	214.17	2.10	2.10	0.00
-11.59	214.17	3.15	3.15	0.00
-10.87	214.20	2.10	2.10	0.00
-10.06	214.20	3.15	3.15	0.00
-10.49	214.22	3.15	2.45	0.22
-11.17	214.23	1.40	1.40	0.00
-11.82	214.27	4.20	3.50	0.17
-10.08	214.27	2.80	2.10	0.25
-10.43	214.27	1.40	1.40	0.00
-10.88	214.30	2.10	1.75	0.17
-6.96	214.42	2.45	2.10	0.14
-11.54	214.43	2.80	1.75	0.38
-9.79	214.51	5.60	5.60	0.00
-10.10	214.51	3.15	2.80	0.11
-10.18	214.56	3.15	2.80	0.11
-9.91	214.57	3.50	2.80	0.20
-9.57	214.62	3.15	3.15	0.00
-9.94	214.66	3.85	3.15	0.18
-6.88	214.71	2.10	1.75	0.17
-10.66	214.71	1.75	1.75	0.00
-10.35	214.78	1.75	1.40	0.20
-8.40	214.82	4.20	3.85	0.08
-11.40	214.87	1.75	1.40	0.20
-10.49	214.87	2.45	2.10	0.14
-11.04	214.88	3.50	2.45	0.30
-11.31	214.92	1.75	1.75	0.00

Table 1 (continued)

Latitude	Longitude	<i>a</i> -diameter (km)	<i>c</i> -diameter (km)	Flatness (km)
-11.38	214.92	1.40	1.40	0.00
-8.46	214.93	3.50	3.15	0.10
-11.12	214.94	4.90	3.85	0.21
-11.45	214.96	3.15	2.80	0.11
-9.92	214.99	2.45	2.10	0.14
-9.92	214.99	2.45	2.10	0.14
-10.44	215.18	3.15	2.80	0.11
-8.26	215.39	3.15	3.15	0.00
-10.77	215.46	2.10	2.10	0.00
-10.95	215.62	2.45	2.10	0.14
-7.57	215.67	4.20	4.20	0.00
-10.61	215.72	2.10	2.10	0.00
-10.70	215.73	2.45	2.45	0.00
-7.73	215.86	2.10	2.10	0.00
-10.28	215.88	1.75	1.75	0.00
-7.71	216.03	2.45	2.10	0.14
-7.77	216.07	3.15	2.10	0.33
-8.41	217.17	2.10	1.75	0.17
-8.55	217.27	1.75	1.40	0.20
-8.50	217.37	2.45	2.45	0.00
-7.51	217.42	2.80	2.80	0.00
-7.59	217.45	3.50	2.45	0.30
-10.59	217.57	3.50	3.50	0.00
-7.53	217.60	2.45	2.10	0.14
-7.15	217.67	2.45	2.10	0.14
-6.46	217.74	1.75	1.40	0.20
-8.13	217.76	1.40	1.40	0.00
-7.18	217.86	2.80	2.45	0.13
-6.39	217.87	1.40	1.40	0.00
-6.53	217.90	1.75	1.75	0.00
-10.82	217.97	3.50	3.50	0.00
-10.68	218.04	1.40	1.05	0.25
-8.10	218.07	2.10	2.10	0.00
-7.09	218.10	2.10	2.10	0.00
-8.64	218.15	1.40	1.05	0.25
-8.61	218.16	1.40	1.40	0.00
-8.68	218.17	1.75	1.75	0.00
-10.30	218.26	2.45	2.45	0.00
-10.36	218.29	3.15	3.15	0.00
-10.32	218.38	3.15	2.80	0.11
-9.69	218.38	2.10	2.10	0.00
-10.82	218.48	2.45	2.45	0.00
-9.98	218.49	2.10	2.10	0.00
-7.41	218.51	1.75	1.40	0.20
-10.73	218.55	2.10	1.75	0.17
-10.48	218.58	3.50	2.80	0.20
-9.74	218.63	3.50	2.80	0.20
-9.44	218.63	3.15	2.80	0.11
-10.96	218.92	2.10	1.75	0.17
-10.27	218.95	1.40	1.40	0.00
-10.35	218.96	1.05	1.05	0.00
-8.10	219.14	2.80	2.10	0.25
-8.20	219.26	2.80	2.80	0.00
-9.10	219.31	5.60	4.20	0.25
-7.96	219.54	3.50	3.50	0.00
-9.35	219.64	4.55	4.20	0.08
-10.29	219.68	1.40	1.40	0.00
-9.34	219.86	3.85	3.85	0.00
-8.86	219.99	2.80	2.80	0.00
-8.86	220.16	2.45	2.45	0.00
-8.60	220.20	4.90	4.55	0.07
-10.58	220.55	2.45	1.75	0.29
-8.85	220.57	2.10	1.75	0.17
-7.74	220.61	4.55	4.20	0.08
-8.55	220.66	1.40	1.40	0.00
-8.62	220.67	1.40	1.05	0.25
-7.73	220.70	2.45	2.10	0.14
-8.31	220.76	2.10	2.10	0.00
-7.73	220.80	2.80	2.45	0.13
-8.79	220.98	2.45	2.45	0.00
-9.21	220.99	4.20	4.20	0.00
-8.04	221.00	2.45	2.10	0.14
-9.91	221.42	1.40	1.40	0.00
-10.02	221.44	2.10	2.10	0.00
-9.87	221.57	1.75	1.75	0.00
-8.92	221.60	1.75	1.40	0.20
-9.18	221.95	4.55	3.85	0.15
-9.06	222.01	4.20	3.85	0.08
-9.15	222.13	3.50	3.15	0.10

Table 1 (continued)

Latitude	Longitude	a-diameter (km)	c-diameter (km)	Flatness (km)
-9.25	222.19	4.55	3.85	0.15
-10.51	222.29	2.80	2.45	0.13
-9.91	222.47	2.10	2.10	0.00
-6.87	222.52	3.85	3.15	0.18
-9.06	222.56	2.80	2.45	0.13
-9.18	222.59	3.50	3.15	0.10
-7.43	222.67	2.80	2.45	0.13
-9.15	222.70	4.20	3.50	0.17
-9.32	222.73	2.45	2.10	0.14
-8.92	222.80	2.45	2.10	0.14
-9.35	222.91	2.10	2.10	0.00
-6.75	222.98	2.10	1.75	0.17
-7.14	223.32	2.45	2.10	0.14
-7.34	223.38	2.80	2.80	0.00
-9.48	223.45	1.40	1.05	0.25
-7.28	223.47	1.75	1.75	0.00
-7.19	223.48	2.45	2.10	0.14
-7.23	223.51	2.10	2.10	0.00
-9.47	223.52	2.80	2.45	0.13
-8.17	223.62	5.25	4.55	0.13
-7.76	223.77	4.20	3.85	0.08
-10.30	224.09	3.15	2.45	0.22
-9.13	224.13	4.20	4.20	0.00
-8.73	224.24	3.15	2.80	0.11
-9.87	224.47	2.45	2.45	0.00
-8.33	224.52	1.75	1.40	0.20
-7.25	224.79	3.50	2.80	0.20
-8.59	224.85	3.15	2.80	0.11
-7.26	225.00	4.20	3.50	0.17
-7.45	225.07	4.55	4.55	0.00
-8.48	225.08	4.90	4.55	0.07
-7.77	225.17	4.20	3.50	0.17
-8.41	225.18	3.50	3.15	0.10
-8.59	225.63	4.20	3.15	0.25
-8.48	225.66	3.15	3.15	0.00
-8.86	225.68	3.15	2.80	0.11
-8.61	225.79	2.80	2.80	0.00
-6.56	225.87	1.75	1.40	0.20
-6.78	225.88	2.10	2.10	0.00
-7.66	225.92	1.40	1.40	0.00
-8.56	226.20	2.80	2.45	0.13
-9.84	226.22	1.40	1.40	0.00
-8.68	226.23	3.50	3.50	0.00
-8.42	226.28	2.45	2.45	0.00
-8.52	226.32	3.15	3.15	0.00
-8.63	226.35	4.55	3.85	0.15
-7.69	227.05	1.40	1.40	0.00
-9.27	227.29	3.15	2.10	0.33
-6.75	227.39	1.75	1.40	0.20
-7.47	227.55	2.10	2.10	0.00
-7.37	227.83	2.80	2.80	0.00
-6.66	228.03	4.55	4.20	0.08
-6.55	228.08	4.20	3.85	0.08
-6.11	228.09	4.55	3.85	0.15
-6.65	228.15	4.55	4.20	0.08
-6.47	228.27	3.15	2.80	0.11
-6.49	228.55	3.15	3.15	0.00
-7.57	228.66	3.50	2.80	0.20
-7.46	228.72	2.45	2.10	0.14
-7.60	228.78	2.80	2.80	0.00
-7.71	228.84	1.40	1.40	0.00
-7.53	228.84	2.45	2.10	0.14
-7.70	228.91	2.80	2.45	0.13
-7.73	229.10	3.50	3.15	0.10
-7.99	229.13	1.75	1.40	0.20
-8.71	229.18	1.40	1.40	0.00
-7.91	229.19	1.40	1.05	0.25
-7.86	229.23	1.05	1.05	0.00
-7.94	229.25	1.40	1.05	0.25
-8.63	229.26	1.75	1.40	0.20
-7.77	229.29	2.10	1.75	0.17
-7.80	229.55	2.10	1.75	0.17
-8.99	229.55	3.15	3.15	0.00
-7.70	229.63	2.10	1.75	0.17
-7.97	229.67	6.30	6.30	0.00
-7.75	229.68	2.10	2.10	0.00
-9.05	229.69	2.80	2.80	0.00
-9.12	229.84	1.75	1.75	0.00

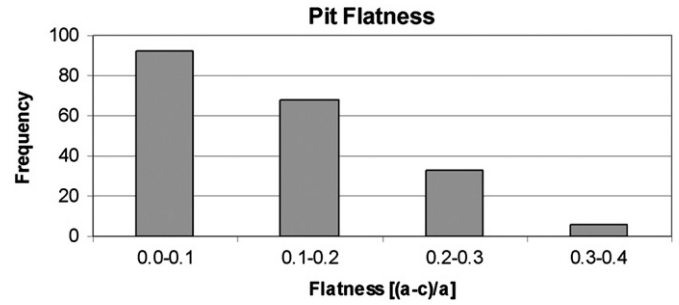


Fig. 2. Histogram of pit flatness, a measure of the circularity. Flatness is calculated as $(a-c)/a$ where a is the long diameter and c is the short diameter of each pit. Over 90% of the pits are circular, while the rest are nearly circular.

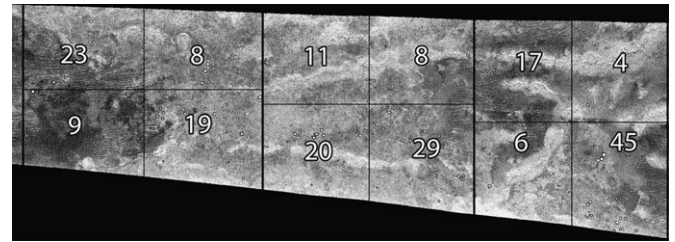


Fig. 3. Chi-squared analysis of pit distribution. The T8 swatch was split into three sections of equal area to create a geometry suitable for analysis. The numbers for each box represent the count of pits for that box. Clustering is apparent, with the largest cluster in the lower right corner.

3. Distribution and size analysis

For the identified pits, we first use Pearson chi-square analysis to assess the randomness of their distribution. Then, we employ fractal analysis, to find the number of pits per unit area, for an additional comparison of the distribution of pits to random distributions. This will quantitatively determine how the number of pits increases with increasing area, thus the plan form and degree of linearity. Next, we analyze the size distribution of pits, comparing diameters regionally. Also, the observed pit diameters are compared with the results of models for random pit development and evolution. With the observed pit distribution and sizes, we assess their potential contribution to Titan's hypsography.

3.1. Chi-squared analysis

An initial look at identified pits suggests a degree of clustering, so to assess the randomness of the pit distribution, and the influence of clustering, we perform a chi-squared analysis. The T8 swatch that contains the 199 identified pits was divided into three sections, each with four sub-sections, all with approximately equal area (Fig. 3). This makes the geometry of the swatch more suitable for analysis.

We use the equation

$$\chi^2 = \sum(O_k - E_k)^2 / E_k \quad (1)$$

for χ^2 (where O_k is the number of pits in the box and E_k is the average number of pits in the boxes) (Taylor, 1997). A reduced χ^2 value is found by dividing by the degrees of freedom ($n-1$) and is used to find the probability of randomness (Table D in Taylor, 1997).

Performing this analysis for the three sections, we find the left section (in Fig. 3) has a 1.1% probability of being a random distribution, the middle section has a 0.15% probability of randomness, and the right section has less than a 0.05% probability of randomness. The densest box of pits, located in the lower right subsection of the right portion of the T8 image, was expanded to

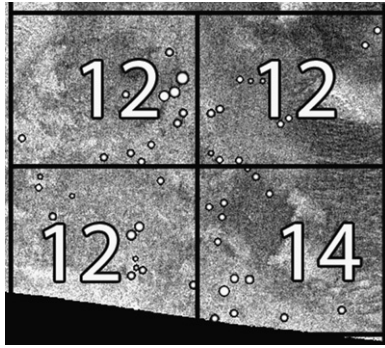


Fig. 4. Chi-squared analysis of pit distribution within the largest cluster, in the south-east corner of pits from Fig. 3, including adjacent pits. The numbers for each box represent the count of pits for that box. Analysis shows a random distribution with no internal clustering.

include adjacent pits giving a total of 50 (Fig. 4). A chi-squared test of this cluster shows a probability of randomness in excess of 99%.

The T8 swath on Titan's equator cannot be covered with boxes of exactly the same size. Examining the consequences of the only approximate similarity of box size, we find in Fig. 3 that the analyses for the left and center regions would not be affected, as area differences could only be compensated with fractional pits. We prefer to work with whole numbers of pits, "integer pits". For the right third of the region, however, the lower right box clearly exceeds the others in size, 6.4% larger than the average for this third. Thus its pit count of 45 should be lowered by 3 and each of the other three boxes would gain a pit. However the re-calculated chi-squared test of the right section still has less than a 0.05% probability of being random. For the densest box of pits (Fig. 4), located in the lower right subsection of the right portion of the T8 image, the slight differences in areas range from 1 to 7%, so do not affect the "integer pit" count.

In summary, chi-squared analyses of 199 pits in Titan's equatorial region (Fig. 3) shows clustering throughout the entire pit field. However, the distribution within the densest pit cluster of 50 pits (Fig. 4) appears to be random).

3.2. Fractal analysis

Pit chains commonly occur on solar system bodies such as Mars (Wyrick et al., 2004). Although lines or chains of pits are not obvious on Titan (Figs. 1 and 6) we undertake fractal analysis to assess the degree of linearity. Fractal analysis is used to objectively assess any subjective perception of whether pits occur in chains or more random groupings. We do this by starting at the center of longitude and latitude of each grouping of pits, then expanding out from that location with circular caps of increasing radius and area and counting the number of pits in each cap (Jurdy and Stefanick, 1990). This gives a cumulative distribution. For a random distribution, the number would increase proportional to the area of the cap. However, for points aligned in strings or chains, the number would increase as the radius of the cap, and thus as the square root of the area. This holds for caps small as compared with Titan's radius. The increase of pits with area then would differentiate the plan form of pits.

For the fractal analysis, we form the cumulative distribution of points $N(A)$ and fit a power law

$$N(A) = CA^{d/2} \quad (2)$$

where d is the fractal dimension, A is the area and C describes the local density of points (Feder, 1988). We estimate these parameters by taking logarithms, plotting (Figs. 5 and 6) and fitting a

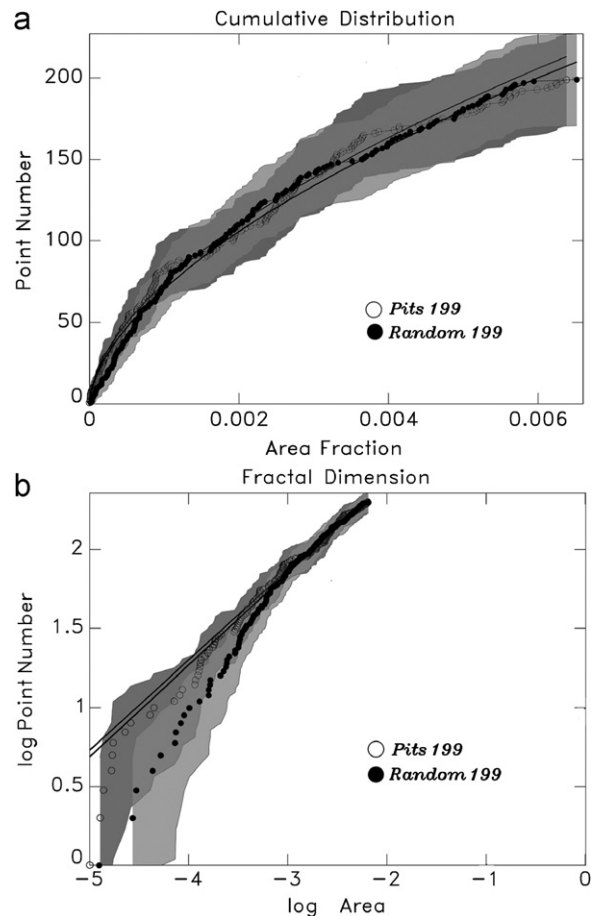


Fig. 5. Fractal analysis of 199 pits found in the T8 image compared with a random set of 199 points. (a) cumulative distribution and (b) logarithmic distribution. The slope of the logarithm for the random set, as well as the observed pits, gives a fractal dimension just over 1.0. Errors of $2\sqrt{N}$ are shaded.

straight line to

$$\log N(A) = \log C + d/2 \log A \quad (3)$$

The number, $N(A)$, over a given area will show some statistical fluctuation, $\pm \sqrt{N(A)}$. In our analysis, we compare the number of pits as a function of area fraction with the same number of random points. Thus, we attempt to quantitatively – and objectively – assess the degree of linearity of Titan's pit distribution.

A total of 199 pits were identified with 50 pits in the largest cluster to the southeast (Fig. 1). An analysis of the entire pit area was compared to a randomly generated set of 199 points with cumulative and logarithmic distributions shown in Fig. 5, with an error of $2\sqrt{N}$ (with N being the number of pits). Over the entire pit field the observed distribution – though slightly more linear than the random set – does not differ from the random points at a statistically significant level. The slope of the logarithm for the random set (Fig. 5b), as well as the observed pits gives a fractal dimension just over 1.0. Unfortunately, the linear strip used for analysis did not contain enough area to the north and south to allow for the expanding circular cap. So the fractal dimensions determined were dominated by the limited area for analysis, a consequence of the linear strip, the swath of data. Here we compare the cumulative distribution for the 199 pits with a best-fitting power law having an exponent of 1.14 (shown as a black line threading through the points). The maximum deviation for the cumulative distribution of the entire set of 199 pits with the cumulative distribution for a power law is 10. Using standard Kolmogorov–Smirnov statistics to compare these cumulative

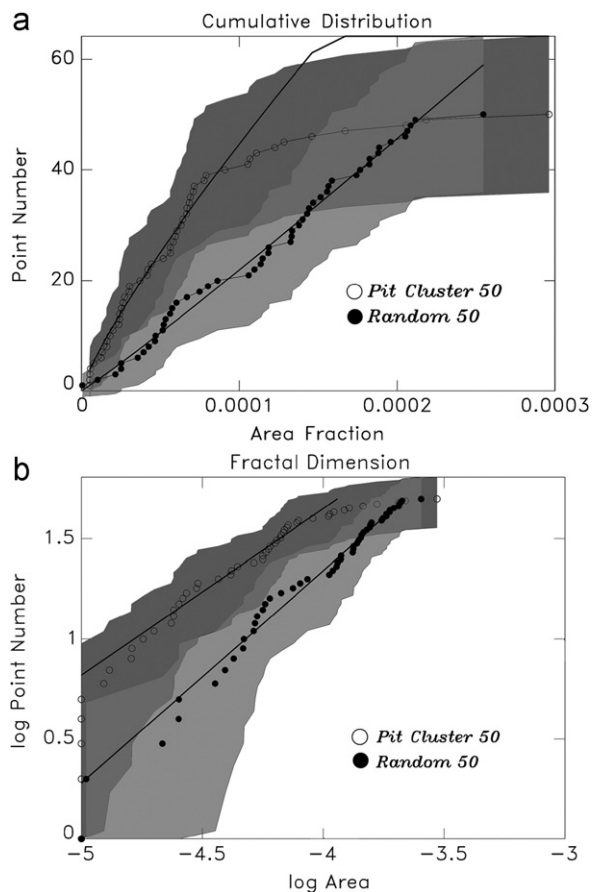


Fig. 6. Fractal analysis of a the densest concentration of 50 pits found in the south-east pit area compared with a random set of 50 points. (a) cumulative distribution and (b) logarithmic distribution. The fractal dimension of the random set is determined as 2.12, slightly over the value of 2.0 expected for a random set. The value for the pit distribution does significantly deviate from that of the random points, giving a dimension of 1.66. Errors of $2\sqrt{N}$ are shaded.

distributions (Press et al., 1992), we find that this small deviation establishes that the power law fit very nearly matches the observed distribution of 199 pits.

Next, we focus on the distribution of pits within the largest cluster. Here we repeat the fractal analysis for the 50 pit cluster in comparison with a randomly generated set of 50 pits, with the cumulative and logarithmic distributions shown in Fig. 6. Here the analysis region is not limited by the dimensions of the swath. In this cluster we find that the observed distribution of pits deviates by more than two standard deviations from the random set with error region shaded ($2\sqrt{N}$). The fractal dimension of the random set is determined as 2.12, slightly over the value of 2.0 expected for a random set. The value for the pit distribution does significantly deviate from that of the random points, giving a dimension of 1.66. Using this dimension, we find a power law with a dimension of 1.66 (shown as the curves in Fig. 6) fits the data very well, with only slight deviations from the cumulative curve. For the cluster of 50 pits, there is a maximum deviation of 4 with the power law curve. With standard Kolmogorov-Smirnov statistics we compare these cumulative distributions (Press et al., 1992) as a measure of fit; we find that the power law fit closely matches the observed pit distributions.

In summary, the fractal analysis for the entire set of 199 pits in the T8 swath shows no strong evidence of linearity or strings for the whole set of 199 pits. But this largely results from the dimensions of the T8 swath. However, the southeast region containing 50 pits exhibits a more linear trend than the random

set. The discrepancy between results for the cluster and the entire set of pits over the swath, suggests that the cluster may be in a different stage of pit development or there could be some local control such as ongoing extension with further thinning. So fractal and other distribution analyses should be performed over smaller sets or groupings in areas contained within the swath.

3.3. Size distribution

The diameter of each pit was found by counting the number of pixels across the pits and then converting to kilometers (Table 1). For the image resolution of 128 pixels/degree there are 0.351 km/pixel. For consistency, a -diameters are used for all size distribution analyses. To assess our initial impression that pit size is unrelated to location, we generated pit-size distribution histograms, dividing the swath into northern and southern parts, and compared the distributions of the halves (Fig. 7). The northern hemisphere shows an average of 2.74, while the southern hemisphere shows an average of 2.76. A t -test (Croxtton, 1953) utilized to determine the estimated standard error for the difference between the two area means yields a t -value of 0.17. This corresponds to a probability of 0.86, implying that the difference between the northern and southern hemisphere diameter distributions is non-significant.

The analysis was repeated with a sliding box histogram from west to east (Fig. 8). A change in the number of pits is evident in the histogram, but it is not clear if there is a change in the distribution. A quartile analysis on each section is performed to provide a useful characterization of the range of values for a set. In quartile analysis the values range from q_0 to q_4 . The lowest fourth of the values range from q_0 to q_1 , the next fourth of the values range from q_1 to q_2 , similarly the third quarter range from q_2 to q_3 , and the final, top quarter range from q_3 to q_4 . The numbers q_1 and q_3 are often referred to as the first and third quartiles, and q_2 is usually referred to as the median. The numbers q_0 and q_4 are the minimum and maximum values. For a set with a statistically defined “normal distribution” the quartiles can be related to the standard deviation: for a normal (or Gaussian) distribution, 68.3% of the values lie within one

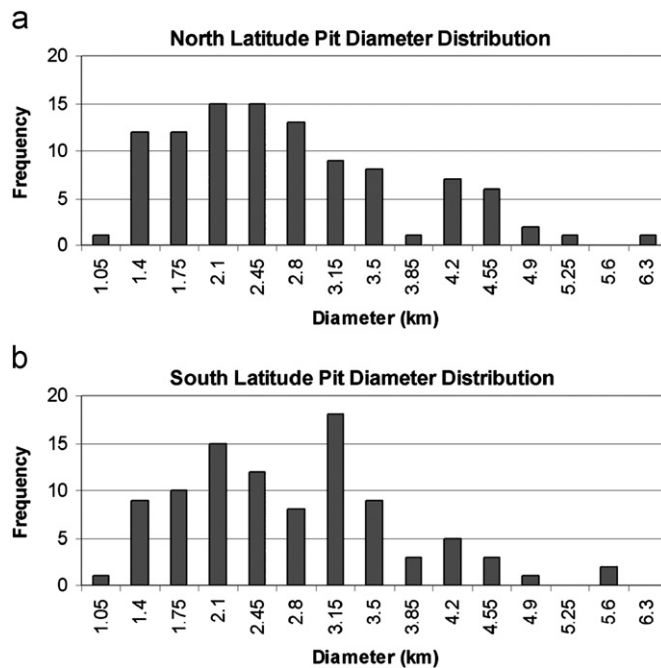


Fig. 7. A comparison of pit size distribution of the north and south halves of the pit field. (a) North latitudes and (b) south latitudes.

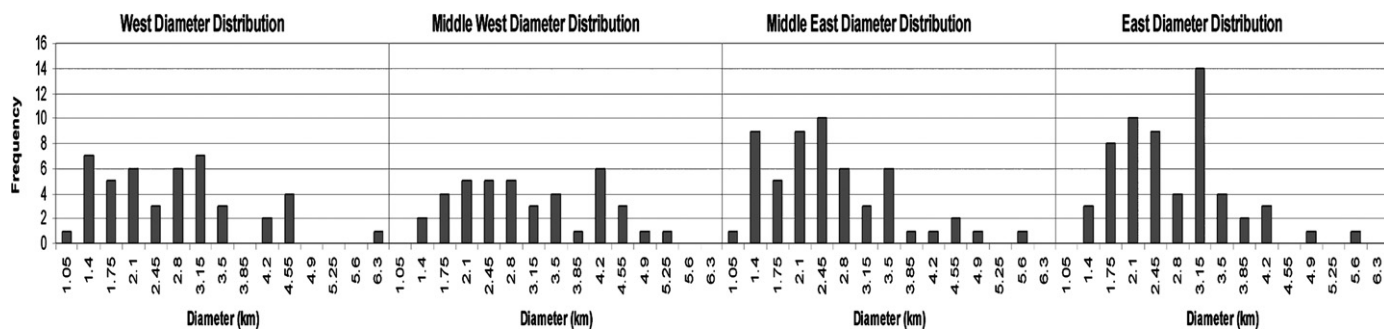


Fig. 8. A sliding box comparison of pit size distributions from west to east across the pit field. Pit diameters from west to east average 2.7 km, 2.6 km, 3 km, and 2.7 km respectively. A quartile analysis shows 50% of the pit diameters lie between 2.1 and 3.15 km, within 0.675 standard deviations of the mean. The middle west section varies more from 2.1 to 4.2 km for 50% of the pits in this area.

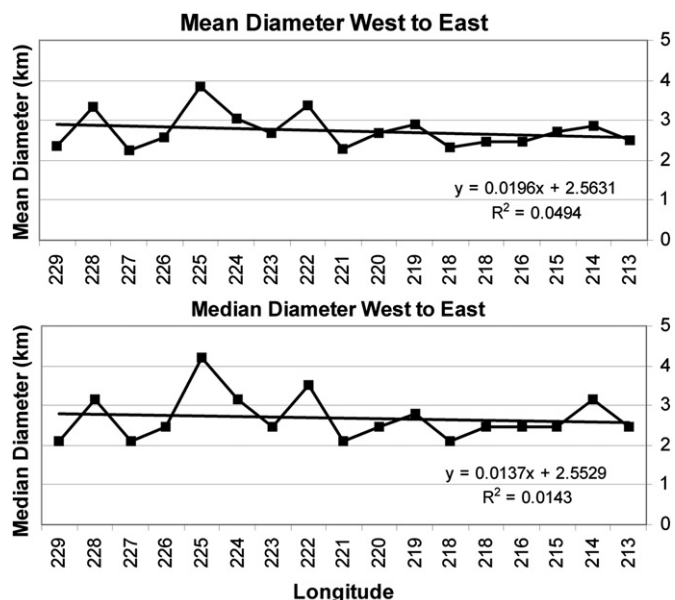


Fig. 9. A graph of mean (top) and median (bottom) pit diameters over equal areas across the pit field. A slope of less than 1 shows no significant change in pit diameters across the pit field.

standard deviation of the mean. Alternatively, the range between the first and third quartiles contains 50% of the values and the points are within 0.675 standard deviations of the mean (Fisher, 1973).

Applying this simple, yet informative analysis to our distributions we find that, in all but the middle west section, 50% of the pit diameters lie between 2.1 and 3.15 km, within 0.675 standard deviations of the mean. The middle west section varies more from 2.1 to 4.2 km for 50% of the pits in this area. A slight skew in pit diameters can be seen in the histogram for this region (Fig. 8). Pit diameters from west to east average 2.7 km, 2.6 km, 3 km, and 2.7 km respectively. Slightly larger pits in the middle west section may show a clustering of large pits in this area. To take a closer look at pit diameters across the longitudinal range and to look for clustering of large pits, we calculated the mean and median diameters over 17 equal areas. A graph of the median and mean diameters as a function of longitude can be seen in Fig. 9. A linear fit of the data shows only a slight decrease in diameter from west to east, with a slope less than 1 for each graph. This is further proof of the lack of a relationship between diameter and pit location.

How different are these four distributions shown in Fig. 8? Here we again use Kolmogorov–Smirnov statistics to compare the

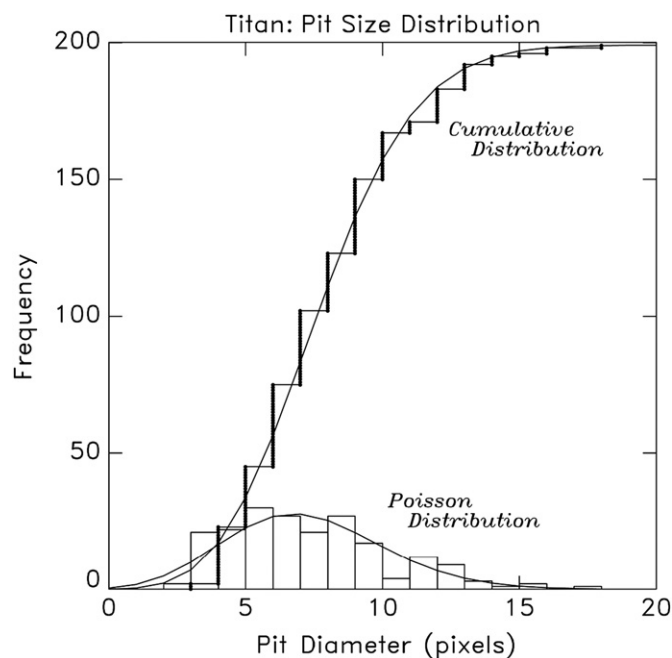


Fig. 10. Histogram of pit diameters in pixels (shown as boxes). Poisson distribution can be seen as smooth line overlaying the histogram. The cumulative distribution for the identified pits is represented by the step function fit by the model curve. Note the similarity to the Poisson distribution and the lack of smaller pits, less than 1 km, due to the restriction of image resolution. An average pit diameter is 2.75 km (8 pixels), while the peak pit diameter is roughly 2.1 km (6 pixels).

distributions. Starting with the histograms we form cumulative distributions and look for the extreme deviations between the distributions for each of the histograms. In this case, the greatest differences are between the cumulative distributions of the second and fourth (furthest east) sections, where $D=.2$. Based on this deviation of .2 and the number of pits in the second (40) and fourth (44) sections and consulting a table for Kolmogorov–Smirnov distributions, we find that a larger deviation would be expected 38% of the time. Thus, the differences in the histograms for pit size versus location are not remarkable.

A histogram of pit diameter versus frequency was employed to determine the incidence of pit diameters (Fig. 10). An average pit diameter was found to be around 2.75 km (eight pixels), while the peak pit diameter is roughly 2.1 km (six pixels). The distribution of pit sizes can be nicely fit with a Poisson curve. We test the degree of fit with Kolmogorov–Smirnov statistics (Press et al., 1992), finding the maximum difference between the cumulative distribution and the Poisson fit at a diameter of about five pixels.

This maximum deviation between the two cumulative curves, scaled by the number of pits, 199, establishes a Kolmogorov–Smirnov distribution. The K–S statistic establishes that there is a reasonable degree of fit between the histogram of the observed pit sizes and the Poisson distribution.

A slight difference in the chi-squared analysis as well as fractal analysis for the largest cluster found in the lower right of the cropped T8 swath (Fig. 1) leads to the question of whether there is a difference in the diameter of the pits in this area compared to the entire swath. A diameter versus frequency histogram of the 50 pits found in the cluster was utilized to determine the pit size distribution for this region (Fig. 11). Average pit diameters were found to be 2.68 km, with a median of 2.45 km. A *t*-test to compare the size distribution of the cluster to the entire swath yields a probability of 0.65, implying that the difference between the cluster and the entire swath area is non-significant.

We constructed a model for pit evolution to establish whether the observed distribution of pit sizes could be replicated with simple starting assumptions. In our model, for a geographical area equivalent to the T8 swath for Titan, we generated 199 points at random locations with random sizes between 1 and 10 pixels. All “pits” smaller than 2 km were eliminated—as if any this small were to exist they would elude identification. Furthermore, any “pit” that fell within the radius of a nearby existing “pit” would be

merged into a single larger “pit”, so features greater than 10 pixels could develop. In reality, coalescing pits would tend to occur where pits clustered, with the pits formed earlier gaining in size. In our model, random locations are specified, with no clustering. Even with this rather simple random model, the generated distribution for randomly evolving pits (Fig. 12) resembles the observed distribution (Fig. 10). Conversely, models that would start with pits having exactly the same diameter could not evolve to a Poisson or Gaussian distribution. In numerical experiments we compare distributions for three different random models and find a variety in their respective histograms for sizes. Yet each of these random sets displays some pits larger than 10 pixels, a result of coalescing of nearby pits. Thus we conclude that a region simulating Titan’s T8 swath, even with 199 random points, would result in some overlap, thus enlarged pits. However, another model, one in which pits exert an influence over a region twice their radius, results in very large pits, with some exceeding 20 pixels in diameter. This does not match observations. A more realistic model might include the effects of pit evolution with time, size loss or perhaps gain, as new pits arrive. Or possibly the initial size distribution might be specified to be Gaussian or some other distribution. Such models are beyond the scope of this paper, and perhaps not even warranted, as we do not yet clearly understand the mechanism of pit formation and their evolution.

4. Discussion

Cassini’s radar imaging revealed nearly 200 dark circular features, interpreted as pits, in Titan’s equatorial region. We have identified and analyzed the spatial distribution of pits along the T8 swath, between 6°–12° south and 212°–230° west. The swath was divided into three sections for chi-squared analysis. The analyses confirmed clustering of pits over the entire pit field (Fig. 4). However, within the southeastern cluster of pits, the densest pit area, the distribution does appear to be random.

Pits on solar system bodies commonly occur in chains. To quantitatively assess the degree of linearity, fractal analysis was performed on the entire set of 199 pits, as well as the densest cluster of 50 in the southeast. Although the entire data set could not be differentiated from a random set of the same size, the cluster showed statistically significant departure from the random set, including the associated errors. This suggests there may be a degree of linearity in the pits, perhaps even remnants of chains. If pit distributions in other clusters, yet to be identified and analyzed, also display a degree linearity, this could be indicative of the pit formation process on Titan.

In addition, pit diameters were estimated. Unfortunately, the number of pits smaller than 1.05 km in diameter cannot be estimated, as these fall below three pixels, below the limit of identification. Pits range in diameter from 1 km to 6.3 km, with an average of 2.75 km. Size distribution analysis shows that pit diameter does not strongly depend on pit location (Figs. 7 and 8). Comparing the cumulative distributions of histograms for subsets of pits by location, no regional difference could be detected in Titan’s pit-size distribution. A simple model for random pit generation was found to simulate the observed Poisson distribution of pit sizes. In this model, a few large pits could develop as features overlap.

Pits are generally located between mountain chains (Radar bright linear features seen in Fig. 1), although some lie outside this region in close proximity to the mountains. This suggests the possibility of a process of pit development associated with formation of these mountains. What causes pits to develop in this area on Titan? Several mechanisms for pit chain development outlined by Wyrick et al. (2004) have been discounted due to

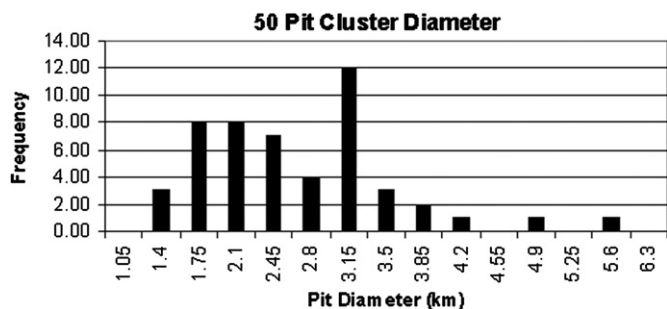


Fig. 11. Histogram of pit diameter frequency, in kilometers, for the 50 pit cluster. An average pit diameter is 2.68 km, with a median of 2.45 km.

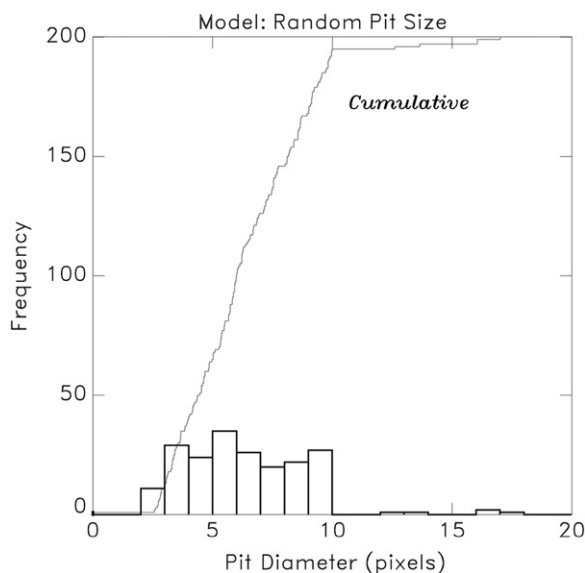


Fig. 12. A model for pit evolution for a geographical area equivalent to the T8 swath for Titan. We generated 199 points at random locations with random sizes between 1 and 10 pixels. All “pits” smaller than 2 km were eliminated. Furthermore, any “pit” that fell within the radius of a nearby existing “pit” would be merged into a single larger “pit”, so features greater than 10 pixels could develop.

Titan's surface composition and state. Cryovolcanism is not probable due to a lack of volcanic features in the area. Secondary craters are not likely as there are no large craters nearby. Sub-parallel mountain chains, identified in this area of the equator and not found to this extent elsewhere on Titan, are possibly due to extension. The coincidence of a large quantity of pits in the same vicinity as the mountains suggests they may be related. Thinning of the crust due to extensional tectonics may facilitate the release of methane hydrates beneath the surface. A sudden release of hydrates could form circular features that we identify as pits. More detailed mapping of this area would aid in a better understanding of pit development on Titan.

We find that in the equatorial region of Titan, specifically the region covered by the equatorial T8 swath (latitudes between 6° – 12° south and longitudes between 212° – 230° west) pits cover $\sim 0.5\%$ of the area. Thus, surface erosion by pit development may contribute to the negative skew observed in Titan's hypsometric curve (Lorenz et al., 2011). The role of pits in the erosional balance can be better evaluated with additional coverage of the Titan to establish the global hypsography and satellite-wide distribution and sizes of pits.

Acknowledgments

We thank the LL Sloss Summer Fellowship for providing funding in 2010. We would also like to thank Steven Jacobsen and Seth Stein for discussion and their comments. We are grateful to Michael Stefanick for assistance with the statistical arguments and modeling. The manuscript was improved with the thoughtful comments of Shane Byrne and an anonymous reviewer.

References

- Atreya, A., Adams, E., Niemann, H., Demick-Montelara, J., Owen, T., Fulchignoni, M., Ferri, F., Wilson, E., 2006. Titan's methane cycle. *Planetary and Space Science* 54, 1177–1187.
- Brown, R.H., Soderblom, L.A., Soderblom, J.M., Clark, R.N., Jaumann, R., Barnes, J.W., Sotin, C., Buratti, B., Baines, K.H., Nicholson, P.D., 2008. The identification of liquid ethane in Titan's Ontario Lacus. *Nature* 454, 607–610.
- Byrne, S., Ingersoll, A., 2003. A sublimation model for Martian south polar ice features. *Science* 299, 1051–1053.
- Croxton, F.E., 1953. *Elementary Statistics*. Dover Publications, Inc., New York.
- Elachi, C., IM, E., Roth, L., Werner, C., 1991. Cassini Titan Radar Mapper. *Proceedings of the IEEE* 79, 867–880.
- Elachi, C., Allison, M., Borgarelli, L., Encrenaz, P., Im, E., Janssen, M., Johnson, W., Kirk, R., Lorenz, R., Lunine, J., Muhleman, D., Ostro, S., Picardi, G., Posa, F., Rapley, C., Roth, L., Seu, R., Soderblom, L., Vetrella, S., Wall, S., Wood, C., Zebker, H., 2004. RADAR: the Cassini Titan radar mapper. *Space Science Reviews* 115, 71–110.
- Feder, J., 1988. *Fractals*. Plenum, New York.
- Ferrill, D., Morris, A., Waiting, D., Franklin, N., Sims, D., 2003. Influence of gravity on the geometry of Martian faults (abstract). In: *Proceedings of the Lunar and Planetary Science Conference*, 24, p. 2050.
- Fisher, R., 1973. *Statistical Methods for Research Workers*. Hafner, New York.
- Jurdy, D., Stefanick, M., 1990. Hot spot distribution. *Geographical Research Letters* 17, 1965–1968.
- Kargel, J., 1995. Cryovolcanism on the icy satellites. *Earth Moon Planets* 67, 101–113.
- Lopes, R., Mitchell, K., Stofan, E., Lunine, J., Lorenz, R., Kirk, R., Wood, C., Wall, S., Robshaw, L., Fortes, A., Neish, C., Radebaugh, J., Reffet, E., Ostro, S., Elachi, C., Allison, M., Anderson, Y., Boehmer, R., Boubin, G., Callahan, P., Encrenaz, P., Flamini, E., Francescetti, G., Gim, Y., Hamilton, G., Hensley, S., Janssen, M., Johnson, W., Kelleher, K., Muhleman, D., Ori, G., Orosei, R., Picardi, G., Posa, F., Roth, L., Seu, R., Shaffer, S., Soderblom, L., Stiles, B., Vetrella, S., West, R., Wye, L., Zebker, H., 2007. Cryovolcanic features on Titan's surface revealed by the Cassini Titan Radar Mapper. *Icarus* 186, 395–412.
- Lorenz, R., 2008. The changing face of Titan. *Physics Today* 61, 34–39.
- Lorenz, R., Kraal, E., Asphaug, E., Thomson, R., 2003. The seas of Titan. *Eos* 84, 125–132.
- Lorenz, R., Turtle, E., Stiles, B., Le Gall, A., Hayes, A., Aharonson, O., Wood, C., Stofan, E., Kirk, R., 2011. Hypsometry of Titan. *Icarus* 211, 699–706.
- Lorenz, R., Wall, S., Radebaugh, J., Boubin, G., Reffet, E., Janssen, M., Stofan, E., Lopes, R., Kirk, R., Elachi, C., Lunine, J., Paganelli, F., Soderblom, L., Wood, C., Wye, L., Zebker, H.A., Anderson, Y., Ostro, S., Allison, M., Boehmer, R., Callahan, P., Encrenaz, P., Ori, G., Francescetti, G., Grim, Y., Hamilton, G., Hensley, S., Johnson, W., Kelleher, K., Mitchell, K., Muhleman, D., Picardi, G., Posa, F., Roth, L., Seu, R., Shaffer, S., Stiles, B., Vetrella, S., Flamini, E., West, R., 2006a. The sand seas of Titan: Cassini Radar observations of longitudinal dunes. *Science* 312, 724–727.
- Lorenz, R., Wall, S., Ruffet, E., Boubin, G., Radebaugh, J., Elachi, C., Allison, M., Anderson, Y., Boehmer, R., Callahan, P., Encrenaz, P., Flamini, E., Francescetti, G., Grim, Y., Hamilton, G., Hensley, S., Janssen, M., Johnson, W., Kelleher, K., Kirk, R., Lopes, R., Lunine, J., Mitchell, K., Posa, F., Roth, L., Seu, R., Shaffer, S., Soderblom, L., Stiles, B., Stofan, E., Vetrella, S., West, R., Wye, L., Zebker, H., 2006b. Radar imaging of giant longitudinal dunes: Namib Desert (Earth) and the Belet Sand Sea (Titan). *Lunar & Planetary Science XXXVII*, 1249.
- Lunine, J., Lorenz, R., 2009. Rivers, lakes, dunes, and rain: crustal processes in Titan's methane cycle. *Annual Review of Earth and Planetary Sciences* 37, 299–320.
- MacClune, K., Fountain, A., Kargel, J., MacAyeal, D., 2003. Glaciers of the McMurdo dry valleys: terrestrial analog for Martian polar sublimation. *Journal of Geophysical Research* 108.
- Malin, M., Caplinger, M., Davis, S., 2001. Observational evidence for an active surface reservoir of solid carbon dioxide on Mars. *Science* 294, 2146–2148.
- Mitri, G., Showman, A., Lunine, J., Lopes, R., 2008. Resurfacing of Titan by ammonia-water cryomagma. *Icarus* 196, 216–224. <http://dx.doi.org/10.1016/j.icarus.2008.02.024>.
- Perron, J., Lamb, M., Koven, C., Fung, I., Yager, E., Adamkovic, M., 2006. Valley formation and methane precipitation rates on Titan. *Journal of Geophysical Research-Planets* 111.
- Press, W.H., Teukolsky, S.A., Vetterling, W.T., Flannery, B.P., 1992. *Numerical Recipes in FORTRAN: The Art of Scientific Computing*. Cambridge University Press, Cambridge.
- Radebaugh, J., Lorenz, R.D., Lunine, J.I., Wall, S.D., Boubin, G., Reffet, E., Kirk, R.L., Lopes, R.M., Stofan, E.R., Soderblom, L., Allison, M., Janssen, M., Pailou, P., Callahan, P., Spencer, C., Team, C.R., 2008. Dunes on Titan observed by Cassini Radar. *Icarus* 194, 690–703.
- Radebaugh, J., Lorenz, R., Kirk, R., Lunine, J., Stofan, E., Lopes, R., Wall, S., 2007. Mountains on Titan observed by Cassini Radar. *Icarus* 192, 77–91.
- Stofan, E.R., Elachi, C., Lunine, J.I., Lorenz, R.D., Stiles, B., Mitchell, K.L., Ostro, S., Soderblom, L., Wood, C., Zebker, H., Wall, S., Janssen, M., Kirk, R., Lopes, R., Paganelli, F., Radebaugh, J., Wye, L., Anderson, Y., Allison, M., Boehmer, R., Callahan, P., Encrenaz, P., Flamini, E., Francescetti, G., Gim, Y., Hamilton, G., Hensley, S., Johnson, W.T.K., Kelleher, K., Muhleman, D., Pailou, P., Picardi, G., Posa, F., Roth, L., Seu, R., Shaffer, S., Vetrella, S., West, R., 2007. The lakes of Titan. *Nature* 445, 61–64.
- Strobel, D., 1974. The photochemistry in the atmosphere of Titan. *Icarus* 21, 466–470.
- Tanaka, K., Golombek, M., 1989. Martian tension fractures and the formation of grabens and collapse features at Valles Marineris. In: *Proceedings of the Lunar and Planetary Science Conference*, 19, pp. 383–396.
- Taylor, J., 1997. *An Introduction to Error Analysis: The Study of Uncertainties in Physical Measurements*. University Science Books.
- Thomas, P., Malin, M., Edgett, K., Carr, M., Hartmann, W., Ingersoll, A., James, B., Soderblom, L., Veverka, J., Sullivan, R., 2000. North-south geological differences between the residual polar caps on Mars. *Nature* 404, 161–164.
- Tomasko, M., Archinal, B., Becker, T., Bezard, B., Bushroo, M., Combes, M., Cook, D., Coustenis, A., de Bergh, C., Dafoe, L., Doose, L., Doute, S., Eibl, A., Engel, S., Gliem, F., Grieger, B., Holso, K., Howington-Kraus, E., Karkoschka, E., Keller, H., Kirk, R., Kramm, R., Kuppers, M., Lanagan, P., Lellouch, E., Lemmon, M., Lunine, J., McFarlane, E., Moores, J., Prout, G., Rizk, B., Rosiek, M., Rueffer, P., Schroder, S., Schmitt, B., See, C., Smith, P., Soderblom, L., Thomas, N., West, R., 2005. Rain, winds and haze during the Huygens probe's descent to Titan's surface. *Nature* 438, 765–778.
- Wegener, A., 1966. *The Origin of Continents and Oceans*, fourth ed. Dover Publications, New York.
- Wood, C., Lorenz, R., Kirk, R., Lopes, R., Mitchell, K., Stofan, E., Team, T.C.R., 2010. Impact craters on Titan. *Icarus* 206, 334–344.
- Wood, C., Lunine, J., Lopes, R., Stofan, E., Mitchell, K., Radebaugh, J., 2006. Crateriform structures on Titan. *LPS Abstract # 1659*.
- Wyrrick, D., Ferrill, D., Morris, A., Colton, S., Sims, D., 2004. Distribution, morphology, and origins of Martian pit crater chains. *Journal of Geophysical Research* 109.
- Yung, Y., Allen, M., Pinto, J., 1984. Photochemistry of the atmosphere of Titan—comparison between model and observations. *Astrophysical Journal Supplement Series* 55, 465–506.